Mon. Not. R. Astron. Soc. **000**, 1–12 (2002) Printed 3 June 2005 (MN LATEX style file v2.2)

Gravitational lensing by the truncated isothermal sphere model for cosmological halos. I. Individual lens properties

Hugo Martel⋆ and Paul R. Shapiro†
Department of Astronomy, University of Texas, Austin, TX 78712

Submitted July 29 2002

ABSTRACT

The gravitational lensing properties of cosmological halos depend upon the mass distribution within each halo. The description of halos as nonsingular, truncated isothermal spheres, a particular solution of the isothermal Lane-Emden equation (suitably modified for $\Lambda \neq 0$), has proved to be a useful approximation for the halos which form from realistic initial conditions in a CDM universe. We derive here the basic lensing properties of such halos, including the image separation, magnification, shear, and time-delay. We also provide analytical expressions for the critical curves and caustics. We show how the scale-free results we derive yield scale-dependent lensing properties which depend upon the cosmological background universe and the mass and collapse redshift of the lensing halos, according to the truncated isothermal sphere (TIS) model of CDM halos derived elsewhere. We briefly describe the application of these results to the currently-favored ΛCDM universe.

Key words: cosmology: theory – dark matter – galaxies: clusters: general – galaxies: formation – galaxies: halos – gravitational lensing

1 INTRODUCTION

The gravitational lensing of distant sources has in recent years become one of the most powerful tools in observational cosmology (see, for example, Soucail 2001 and references therein). Since the effects of gravitational lensing depend upon the redshift of the source, the cosmological background, and the distribution of matter in the universe, they can be used to constrain the cosmological parameters and the primordial power spectrum of density fluctuations from which structure originates. In addition, many of the effects produced by gravitational lenses, such as image multiplicity, separations, and time delay, depend strongly upon the matter distribution inside the lenses. Hence, measurements of these effects can provide a unique tool for probing the matter distribution inside collapsed objects like galaxies and clusters, providing the only direct measurement of their dark matter content, and constraining the theory of their formation and evolution.

Until recently, the internal structure of halos adopted in lensing studies was generally some gravitational equilibrium distribution, either singular or nonsingular (e.g., King model, singular isothermal sphere, pseudo-isothermal sphere), not necessarily motivated directly by the theory of cosmological halo formation (see, e.g., Young et al. 1980; Turner, Ostriker, & Gott 1984; Hinshaw & Krauss 1987; Narayan & White 1988; Blandford et al. 1991; Jaroszyński 1991, 1992; Kochanek 1995; Premadi, Martel, & Matzner 1998; Premadi et al. 2001; Rusin & Ma 2001). As the theory of halo formation in the CDM model has advanced in recent years, however, the halo mass profiles adopted for lensing models have been refined to reflect this theory. Numerical simulations of large-scale structure formation in Cold Dark Matter (CDM) universes predict that galaxies and clusters have a singular density profile which approaches a power law $\rho \propto r^{-n}$ at the center, with the exponent n ranging from 1 to 1.5 (Cole & Lacey 1996; Navarro, Frenk, & White 1996, 1997; Tormen, Bouchet, & White 1997; Fukushige & Makino 1997, 2001a,b; Moore et al. 1998, 1999; Huss, Jain, & Steinmetz 1999; Ghigna et al. 2000; Jing & Suto 2000; Klypin et al. 2000; Power et al. 2002). These results are in apparent conflict with observations of rotation curves of dark-matter-dominated dwarf galaxies and low surface brightness galaxies, which favor a flat-density core (cf. Primack et al. 1999; Burkert & Silk 1999; Moore et al. 1999; Moore 2001). On the scale of clusters of galaxies, observations of strong gravitational lensing of background galaxies by foreground clusters also favor the presence of a finite-density core in the centers of clusters (see, e.g., Tyson, Kochanski, & Dell'Antonio 1998).

Several possible explanations have been suggested in order to explain this discrepancy. The rotation curve data might lack sufficient spatial resolution near the center to

⋆ E-mail: hugo@simplicio.as.utexas.edu
† E-mail: shapiro@astro.as.utexas.edu

distinguish unambiguously between a density profile with a flat-density core and one with a singular profile (e.g. van den Bosch & Swaters 2001). Attempts have also been made to improve the numerical resolving power of the simulations to obtain a more accurate determination of the slope of the predicted density profiles at small radii (e.g. Moore et al. 1999; Power et al. 2002). However, if the flat-core interpretation of the observations and the singular cusps predicted by the numerical simulations are both correct, then the simulation algorithms may be ignoring some physical process which would, if included, serve to flatten the halo density profiles at small radii relative to the results for purely gravitational, N-body dynamics of cold, collisionless dark matter, while retaining the more successful aspects of the CDM model. For example, gasdynamical processes (see, e.g. El-Zant, Shlosman, & Hoffman 2001) and a modification of the microscopic properties of CDM, such as the proposal of self-interacting dark matter (Spergel & Steinhardt 2000), both have the potential to lower the central density of halos and possibly reconcile simulations with observations.

Lensing by the two kinds of halo mass profiles, singular versus flat-core, will be different. This has led to attempts to predict the differences expected if the halos have the singular cusp of the NFW or Moore profiles or else a profile with a flat core (e.g. Kochanek 1995; Keeton & Madau 2001; Rusin & Ma 2001; Wyithe, Turner, & Spergel 2001; Takahashi & Chiba 2001; Li & Ostriker 2002). Singular profiles like that of NFW are physically motivated by the N-body simulations, and the latter have been used to place these halo profiles empirically in a proper cosmological context which permits statistical predictions for the CDM model. The nonsingular profiles which have been adopted to contrast with these singular ones, however, are generally no more than parameterized, mathematical fitting formulae, with no particular physical model to motivate them or put them in a proper cosmological context.

We have developed an analytical model for the post-collapse equilibrium structure of virialized objects that condense out of a cosmological background universe, either matter-dominated or flat with a cosmological constant (Shapiro, Iliev, & Raga 1999, hereafter Paper I; Iliev & Shapiro 2001a, hereafter Paper II). This *Truncated Isothermal Sphere*, or TIS, model assumes that cosmological halos form from the collapse and virialization of "top-hat" density perturbations and are spherical, isotropic, and isothermal. This leads to a unique, nonsingular TIS, a particular solution of the Lane-Emden equation (suitably modified when $\Lambda \neq 0$). The size r_t and velocity dispersion σ_V are unique functions of the mass M and formation redshift $z_{\rm coll}$ of the object for a given background universe. The TIS density profile flattens to a constant central value, ρ_0, which is roughly proportional to the critical density of the universe at the epoch of collapse, with a small core radius $r_0 \approx r_t/30$ (where $\sigma_V^2 = 4\pi G\rho_0 r_0^2$ and $r_0 \equiv r_{\rm King}/3$, for the "King radius" $r_{\rm King}$, defined by Binney & Tremaine 1987, p. 228).

Even though the TIS model does not produce the central cusp in the density profile of halos predicted by numerical CDM simulations at very small radii, it does reproduces many of the average properties of these halos quite well, suggesting that it is a useful approximation for the halos which result from more realistic initial conditions (Papers I, II; Iliev & Shapiro 2001b and references therein). In particular, the TIS mass profile agrees well with the fit by NFW to N-body simulations (i.e. fractional deviation of $\sim$ 20% or less) at all radii outside of a few TIS core radii (i.e. outside a King radius or so). It also predicts the internal structure of X-ray clusters found by N-body and gasdynamical simulations of cluster formation in the CDM model. For example, the TIS model reproduces to great accuracy the mass-temperature and radius-temperature virial relations and integrated mass profiles derived empirically from the simulations of cluster formation (Evrard, Metzler, & Navarro 1996). The TIS model also successfully reproduces to high precision the mass-velocity dispersion relation for clusters in CDM simulations of the Hubble volume by the Virgo Consortium (Evrard et al. 2002), including its dependence on redshift for different background cosmologies. The TIS model also correctly predicts the average value of the virial ratio in N-body simulations of halo formation in CDM.

The TIS profile matches the observed mass profiles of dark-matter-dominated dwarf galaxies. The observed rotation curves of dwarf galaxies are generally well fit by a density profile with a finite density core suggested by Burkert (1995), given by

$$\rho(r) = \frac{\rho_{0,B}}{(r/r_c+1)(r^2/r_c^2+1)}\,. \qquad (1)$$

The TIS model gives a nearly perfect fit to this profile, with best fit parameters $\rho_{0,B}/\rho_{0,\rm TIS} = 1.216$, $r_c/r_{0,\rm TIS} = 3.134$, correctly predicting the maximum rotation velocity $v_{\rm max}$ and the radius $r_{\rm max}$ at which it occurs. The TIS model can also explain the mass profile with a flat density core measured by Tyson, Kochanski, & Dell'Antonio (1998) for cluster CL 0024+1654 at $z = 0.39$, using the strong gravitational lensing of background galaxies by the cluster to infer the cluster mass distribution (Shapiro & Iliev 2001). The TIS model not only provides a good fit to the projected surface mass density distribution of this cluster within the arcs, but also predicts the overall mass, and a cluster velocity dispersion in close agreement with the value $\sigma_v = 1150$ km/s measured by Dressler et al. (1999).

Several authors have studied the effect of lensing by halos with a flat-density core (Jaroszyński 1991, 1992; Kochanek 1995; Premadi, Martel, & Matzner 1998; Premadi et al. 2001) or by NFW or Moore profiles that have been generalized, so that the inner slope of the density profile is arbitrary (Keeton & Madau 2001; Rusin & Ma 2001; Wyithe, Turner, & Spergel 2001; Li & Ostriker 2002). These particular density profiles are essentially mathematical conveniences without physical motivation. There is no underlying theoretical model in these cases that was used to predict the value of the core radius or the departure of the inner slope of the density profile from the value found by N-body simulations of CDM. By contrast, the TIS model is based on a set of physical assumptions concerning the origin, evolution, and equilibrium structure of halos in CDM universes. Observations of gravitational lenses have the potential to distinguish between the TIS profile and singular ones like the NFW profile, as several observable properties of gravitational lenses will be strongly affected by the presence, or absence of a central cusp in the density profile. One example of an important observable that can distinguish between various density profiles is the parity of the number of im-

ages. Lenses with nonsingular density profiles, such as the TIS, obey the *odd number theorem*. The number of images of a given source is always odd, unless the source is extended and saddles a caustic (see Schneider, Ehlers, & Falco 1992, hereafter SEF, p. 172). Lenses with singular profiles, like the singular isothermal sphere, the NFW profile, or the Moore profile, need not obey this theorem, even for point sources. Most observed multiple-image gravitational lenses have either 2 or 4 images, and this may argue against profiles with a central core (Rusin & Ma 2001). There are, however, other possible explanations for the absence of a third or fifth image. That image tends to be very close to the optical axis, and might be hidden behind the lens itself. Also, it is usually highly demagnified, and might be too faint to be seen.

We can use the TIS solution to model observed gravitational lenses individually. Alternatively, we can use the observations collectively to constrain the distribution of halo properties as characterized by the TIS solution. These properties, core radius, velocity dispersion, central density, and so on, depend upon the mass of the lensing halos and the redshift at which they form. Observational constraints on the statistical distribution of these properties will, in turn, impose constrains on the cosmological parameters and the primordial power spectrum of density fluctuations.

The problem of studying gravitational lensing of distant sources in an inhomogeneous universe can be divided into two parts. The first part consists of determining the intrinsic properties of the lenses. In particular, we need to determine the relationship between the observables (image multiplicity, magnification, brightness ratio, sheer, image separation, time delay, ...) and the lens parameters. The second part consists of tying the lens properties to the cosmology. This involves using cosmological models of structure formation and evolution to determine the statistical distribution of the lens parameters, the clustering properties of the lenses, and the nature of their environments. In this paper, we focus on the first part, determining the intrinsic properties of individual lenses, which is an essential building block. The second part will be the subject of forthcoming papers.

The remainder of this paper is organized as follows. In §2, we derive the lens equation. In §3, we compute the critical curves and caustics. In §4, we study the properties of multiple images: separation, magnification, brightness ratios, and time delay. In §5, we place the scale-free description of these properties in the cosmological context of the CDM model and explain how the dimensionless parameters of §2–§4 are related by the TIS model to the properties of lensing halos in physical units. Summary and conclusion are presented in §6.

2 THE LENS EQUATION

Figure 1 illustrates the lensing geometry. η and ξ are the position of the source on the source plane and the image on the image plane, respectively, $\hat{\alpha}$ is the deflection angle, and D_L, D_S, and D_{LS} are the angular diameter distances between observer and lens, observer and source, and lens and source, respectively. The lens equation is

$$\eta = \frac{D_S}{D_L}\xi - D_{LS}\hat{\alpha}\,. \tag{2}$$

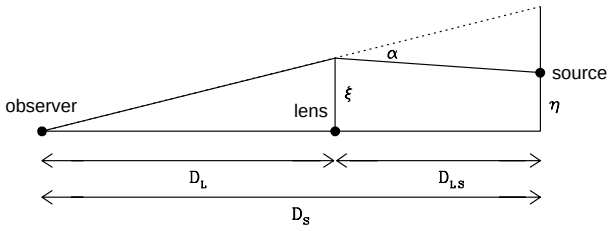

Figure 1. The lensing geometry: the dots indicate the location of the observer, lensing galaxy, and source. r_c is the core radius of the galaxy, and η is the distance between the source and the optical axis. The angular diameter distances D_L, D_{LS}, and D_S are also indicated.

Notice that since the lens is axially symmetric, we can write the quantities η, ξ, and $\hat{\alpha}$ as scalars instead of 2-component vectors. We introduce a characteristic length scale ξ_0, and rescale the positions and deflection angle, as follows:

$$y = \frac{D_L\eta}{D_S\xi_0}\,, \tag{3}$$

$$x = \frac{\xi}{\xi_0}\,, \tag{4}$$

$$\alpha = \frac{D_L D_{LS}\hat{\alpha}}{D_S\xi_0}\,. \tag{5}$$

The lens equation reduces to

$$y = x - \alpha(x)\,. \tag{6}$$

To compute the deflection angle α, we first need an expression for the projected surface density $\sigma(\xi)$. The density profile of the TIS is well-fitted by the following approximation:

$$\rho(r) = \rho_0\left(\frac{A}{a^2 + r^2/r_0^2} - \frac{B}{b^2 + r^2/r_0^2}\right) \tag{7}$$

(Paper I) where $A = 21.38$, $B = 19.81$, $a = 3.01$, $b = 3.82$. The projected surface density is given by

$$\sigma(\xi) = \int_{-\infty}^{\infty}\rho(r)dz\,, \tag{8}$$

where ξ is the projected distance from the center of the TIS, and $z = (r^2 - \xi^2)^{1/2}$. This expression assumes that the fit given by equation (7) is valid all the way to $r = \infty$. Actually, it is only valid up to a truncation radius $r_t \approx 30r_0$ (the actual value is 29.4 for an Einstein-de Sitter universe [Paper I], slightly different for an open matter-dominated universe, or a flat universe with a cosmological constant [Paper II]). One could always set the limits in equation (8) to $\pm(r_t^2 - \xi^2)^{1/2}$. However, it turns out that the change in σ would be small, simply because the value of 30 is significantly larger than both a and b. Also, the density $\rho(r)$ is nonzero at $r > 30r_0$, and ignoring its contribution entirely would be incorrect. For the sake of simplicity, we shall assume that equation (8) remains a good approximation out to $r = \infty$. We substitute equation (7) in equation (8), and get

$$\sigma(\xi) = \pi\rho_0 r_0^2\left[\frac{A}{(a^2r_0^2 + \xi^2)^{1/2}} - \frac{B}{(b^2r_0^2 + \xi^2)^{1/2}}\right] \tag{9}$$

[This result was also derived by Natarajan & Lynden-Bell (1997) and Iliev (2000)]. For spherically symmetric lenses, the deflection angle is given by

$$\alpha(x) = \frac{2}{x}\int_0^x x' \frac{\sigma(x')}{\sigma_{\rm crit}} dx' \tag{10}$$

[SEF, eq. (8.3)], where $\sigma_{\rm crit}$ is the critical surface density, given by

$$\sigma_{\rm crit} = \frac{c^2 D_S}{4\pi G D_L D_{LS}}\,, \tag{11}$$

where c and G are the speed of light and the gravitational constant, respectively, and D_L, D_S, and D_{LS} are the angular diameter distances between observer and lens, observer and source, and lens and source, respectively. We substitute equation (9) into equation (10), eliminate ξ using equation (4), and set the characteristic scale ξ_0 equal to r_0. We get

$$\alpha(x) = \frac{2\pi\rho_0 r_0}{\sigma_{\rm crit} x}\Big[A(a^2+x^2)^{1/2} - B(b^2+x^2)^{1/2} - Aa + Bb\Big]\,. \tag{12}$$

We now introduce the dimensionless central surface density, or central convergence, κ_c, defined by

$$\kappa_c \equiv \frac{\sigma(\xi=0)}{\sigma_{\rm crit}} = \frac{\pi\rho_0 r_0}{\sigma_{\rm crit}}\left(\frac{A}{a}-\frac{B}{b}\right)\,, \tag{13}$$

and use this expression to eliminate $\sigma_{\rm crit}$ in equation (12). It reduces to

$$\alpha(x) = \frac{2ab\kappa_c}{(Ab-Ba)x}\Big[A(a^2+x^2)^{1/2} - B(b^2+x^2)^{1/2} - Aa + Bb\Big]\,. \tag{14}$$

This expression has the following limiting cases:

$$\alpha(x) = \begin{cases} \kappa_c x\,, & x \ll a,\, b\,; \\ \dfrac{2ab(A-B)\kappa_c}{Ab-Ba}\,, & x \gg a,\, b\,. \end{cases} \tag{15}$$

The final form of the lens equation is

$$y = x - \frac{2ab\kappa_c}{(Ab-Ba)x}\Big[A(a^2+x^2)^{1/2} - B(b^2+x^2)^{1/2} - Aa + Bb\Big]\,. \tag{16}$$

[This result was also obtained by Chiba & Takahashi (2001)].

3 CRITICAL CURVES AND CAUSTICS

3.1 Solutions

The determination of the critical curves is quite trivial for axially symmetric lenses. The dimensionless interior mass $m(x)$ is related to the deflection angle $\alpha(x)$ by

$$m(x) \equiv \alpha(x)x = \frac{2ab\kappa_c}{(Ab-Ba)}\Big[A(a^2+x^2)^{1/2} - B(b^2+x^2)^{1/2} - Aa + Bb\Big]\,. \tag{17}$$

[SEF, eq. (8.3)]. Tangential critical curves are defined by

$$\frac{m(x)}{x^2} = \frac{2ab\kappa_c}{(Ab-Ba)x^2}\Big[A(a^2+x^2)^{1/2} - B(b^2+x^2)^{1/2} - Aa + Bb\Big] = 1\,. \tag{18}$$

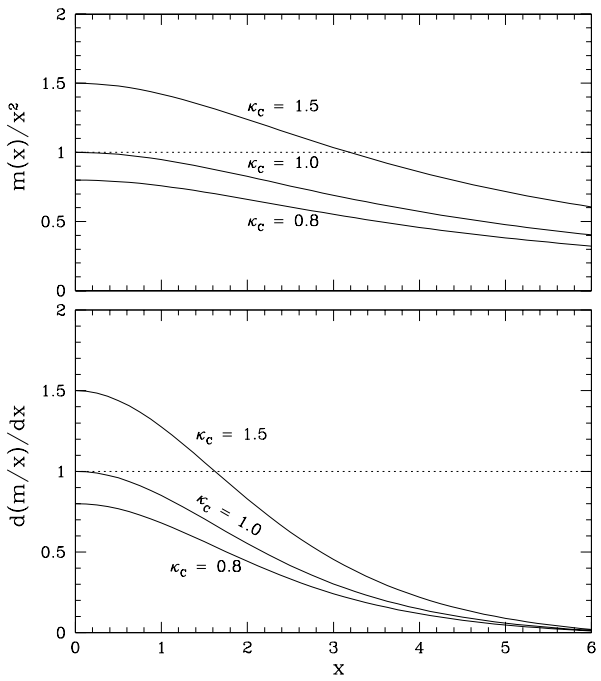

Figure 2. Top: $m(x)/x^2$ versus x, for 3 particular values of κ_c. Tangential critical curves, defined by $m(x)/x^2 = 1$, can only occur for $\kappa_c > 1$. Bottom: $d(m/x)/dx$ versus x, for 3 particular values of κ_c. Radial critical curves, defined by $d(m/x)/dx = 1$, can only occur for $\kappa_c > 1$.

This can be turned into a fourth-degree equation for x^2. Even though such equation can be solved analytically, this is a case where a numerical solution is preferable. But first let us investigate the existence of a solution. According to equations (15) and (17), $m(x) = \kappa_c x^2$ at small x. As x increases, the dependence of $m(x)$ on x drops from $m(x) \propto x^2$ to $m(x) \propto x$. If $\kappa_c < 1$, $m(x)$ "starts up" below x^2 and can never raise above it, and therefore equation (18) has no solution. If $\kappa_c = 1$, equation (18) has a unique solution at $x = 0$. Finally, if $\kappa_c > 1$, there is a unique solution $x > 0$. This is illustrated in the top panel of Figure 2. This result was expected: critical curves are associated with the phenomenon of multiple imaging. For axially symmetric lenses with monotonically decreasing surface density ($d\sigma/d\xi < 0$), multiple images can occur only if $\kappa_c > 1$ (SEF, p. 238).

Radial critical curves are defined by

$$\frac{d(m/x)}{dx} = \frac{2ab\kappa_c}{(Ab-Ba)x^2}\left[-\frac{Aa^2}{(a^2+x^2)^{1/2}} + \frac{Bb^2}{(b^2+x^2)^{1/2}} + Aa - Bb\right] = 1\,. \tag{19}$$

According to equation (15), $d(m/x)/dx = d\alpha/dx = \kappa_c$ at small x. Equation (19) clearly shows that $d(m/x)/dx$ is a monotonically decreasing function of x. Hence, equation (19) has a nonzero solution only if $\kappa_c > 1$. This is illustrated in the bottom panel of Figure 2.

We have solved equations (18) and (19) numerically for the tangential critical radius x_t and radial critical radius x_r. The solutions are plotted in Figure 3, as functions of κ_c. Also plotted is the radial caustic radius y_r, obtained by substi-

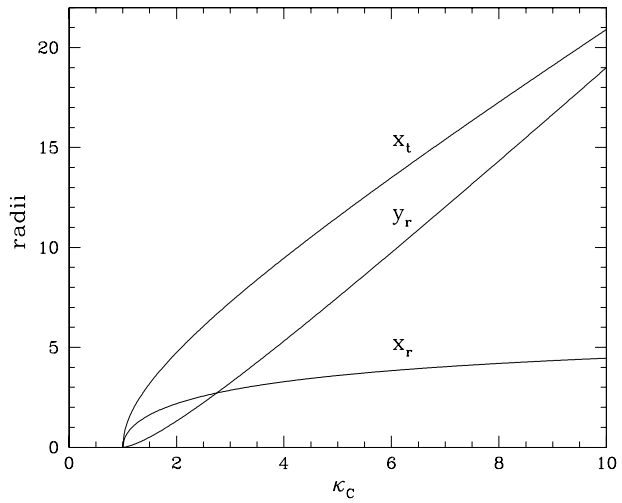

Figure 3. Radii of the radial critical circle, x_r, tangential critical circle, x_t, and radial caustic, y_r, versus κ_c.

tuting the value of x_r into equation (16). (The value of y_r we obtain is actually negative, but this reflects the fact that the equation locates the point in the plane of the sky which is the intersection between the radial caustic circle projected onto that plane and a line in this plane from some point on the radial critical circle through the origin at the center of the lens; the intersection point on the radial caustic circle is on the opposite side of the origin. The actual radius of the caustic circle, then, is the absolute value of y_r in that case.) Both x_t and y_r increase rapidly with κ_c, while the value of x_r levels off. We can easily find the asymptotic behavior in the limit of large κ_c. To find x_t, we take the limit $\kappa_c \rightarrow \infty$ in equation (18). To satisfy this equation, either the factor x^2 in the denominator must diverge, or the quantity in bracket must vanish. But this quantity is zero only for $x = 0$, and approaches 0 as x^2, cancelling the x^2 in the denominator. Hence, the only way to satisfy equation (18) in the limit $\kappa_c \rightarrow \infty$ is by having $x \rightarrow \infty$ in the denominator. We take the limit $x \rightarrow \infty$ in equation (18), and keep the first and second leading terms. We get

$$x = \frac{2ab\kappa_c}{Ab - Ba}\left(A - B + \frac{Bb - Aa}{x}\right) . \qquad (20)$$

Setting $x = \infty$ in the last term, we get $x \approx 2ab(A - B)\kappa_c/(Ab - Ba)$. We then substitute this value in the last term of equation (20), and get

$$x_t = \frac{2ab(A-B)}{Ab-Ba}\kappa_c + \frac{Bb-Aa}{A-B} = 1.638\kappa_c + 7.210\,, \qquad \kappa_c \gg 1\,. \qquad (21)$$

To find x_r, we take the limit $\kappa_c \rightarrow \infty$ in equation (19). In this case, the quantity in brackets first increases with x, then decreases and drops to 0 at a finite value $x = 6.479$. Hence, unlike equation (18), it is the bracket, not the factor of x^2 in the denominator, that prevents the expression from diverging as $\kappa_c \rightarrow \infty$. The asymptotic limit is therefore

$$x_r = 6.479\,, \qquad \kappa_c \gg 1\,. \qquad (22)$$

Finally, we substitute this value of x_r in equation (16), and take the limit $\kappa \rightarrow \infty$. We get

$$y_r = 2.425\kappa_c - 6.479\,, \qquad \kappa_c \gg 1\,. \qquad (23)$$

3.2 Illustrative example

Using a simple ray-tracing algorithm, we computed the image(s) of a circular source of diameter $\Delta y = 1$, created by a TIS with central convergence $\kappa_c = 4.015$. The results are shown in Figure 4 for 8 different locations of the source, ranging from $y = 8.0$ to $y = 0.0$. For each case, the left panel shows the source and the caustic circle ($y_r = 5.640$) on the source plane, and the right panel shows the images(s), the radial critical circle ($x_r = 3.334$), and the tangential critical circle ($x_t = 9.783$) on the image plane. For the cases $y = 8.0$ and 6.0, only one image appears. At $y = 5.4$, the source overlaps the caustic, and a second, radially-oriented image appears on the radial critical circle. At $y = 4.8$, the source is entirely inside the caustic, and the second image splits in two images, located on opposite sides of the radial critical circle, forming with the original image a system of 3 aligned images. As the source moves toward $y = 0$, the central image moves toward $x = 0$ and becomes significantly fainter, while the other images move toward the tangential critical circle and become bright, elongated arcs. At $y = 0$, the two arcs have merged to form an Einstein ring located on top of the tangential critical circle, while the central image, very faint, is still visible in the center.

The central image is always located inside the radial critical curve, which has a maximum radius of 6.479 (eq. [22]). The density profile of the TIS extends to a cutoff radius of order 29.4 (Papers I and II) [Note: We are neglecting here the effect of matter distributed outside the virial radius of our lensing halo.]. Hence the central image is always located "inside" the TIS and will be visible only if the lens is transparent. Incidently, all the images shown in Figure 4 are located inside the TIS, because the value we used for κ_c is rather modest. Setting $x_t = 29.4$ in equation (21), we get $\kappa_c = 17.9$. This is the value of κ_c for which the tangential critical circle is located along the edge of the TIS. For opaque lenses, the image located between the tangential and radial critical circles (leftmost images in Fig. 4) might be visible only if $\kappa_c > 17.9$. For $\kappa_c < 17.9$, only the outermost image, located outside the tangential critical circle, might be visible.

4 PROPERTIES OF MULTIPLE IMAGES

4.1 Image separation

The locations of the images are computed by solving the lens equation (16). After rewriting this equation as $x - y = \alpha(x)$, we can solve it graphically. In Figure 5, we show the multiple image diagram for the particular case $\kappa_c = 5.005$. The solid curves shows $\alpha(x)$, while the dotted lines show $x - y$ for particular values of y. Each intersection between a line and the curve corresponds to one image. If $y > y_r$ (bottom line), the source is outside the caustic circle, and only one image appears. If $y = y_r$ the source is on the caustic circle and a second image appears on the radial critical circle, at $x = -x_r$. For $y < y_r$, the source is inside the caustic, and the

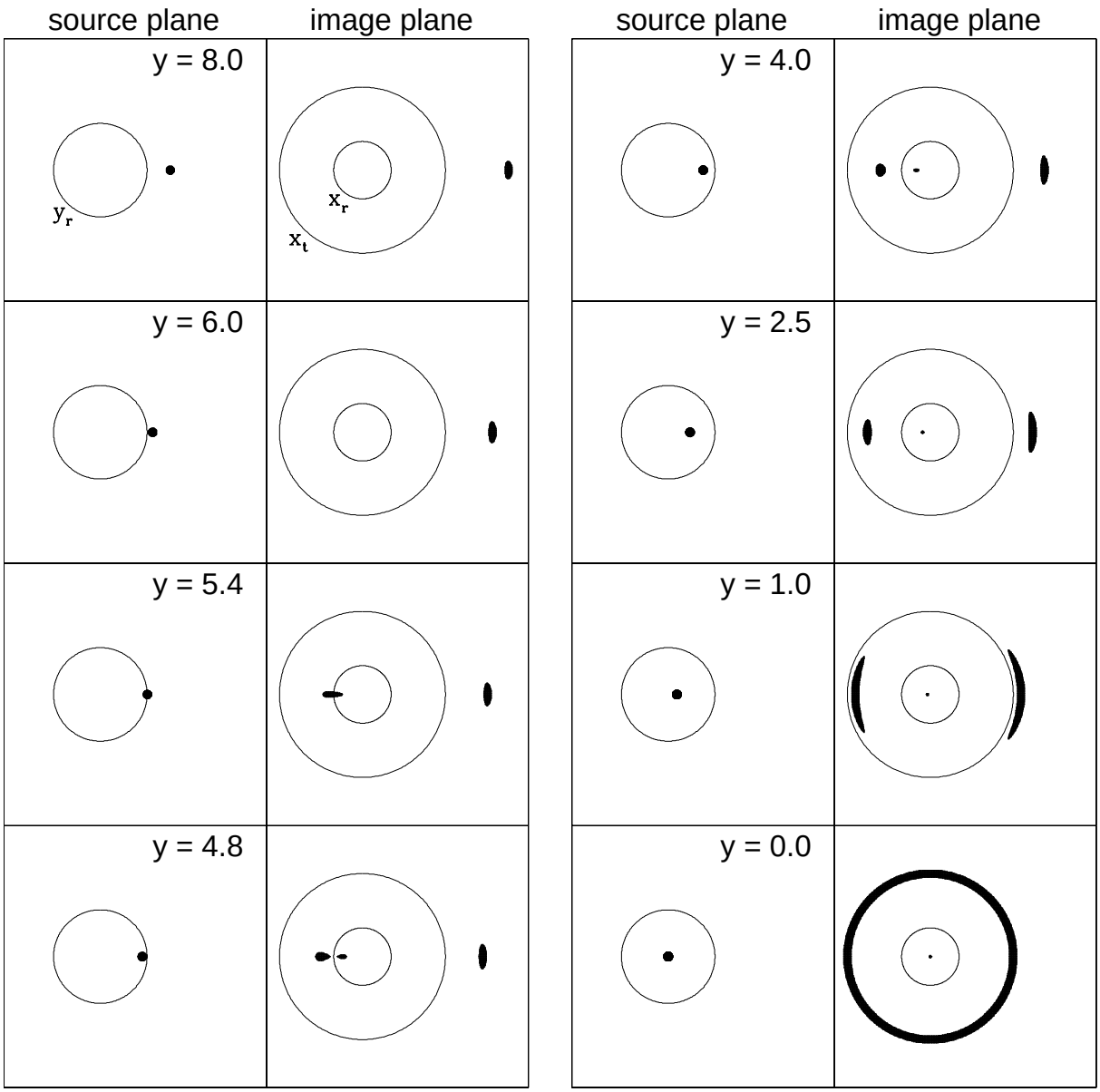

Figure 4. Images of a circular source. Each pair of panels shows the source plane in the left panel, with the caustic, and the image plane in the right panel, with the radial (inner) and tangential (outer) critical circles. The position y of the source on the source plane is indicated. We used $\kappa_c = 4.014$, and a source of diameter $\Delta y = 1$.

second image splits into two images. Finally, for $y = 0$ (top curve), the central image is located at $x = 0$, and the two outer images are located on the tangential circle, at $x = \pm x_t$. Actually, these two images merge to form an Einstein ring. The slope of the curve $\alpha(x)$ versus x is equal to κ_c at $x = 0$. It is clear from Figure 5 that if we lower κ_c below 1, any $x-y$ versus x line will intersect the curve only once; multiple images cannot occur if $\kappa_c < 1$. In Figure 6, we plotted the solution of the lens equation for various values of κ_c. The bifurcation from 1 to 3 images is clearly visible on all panels with $\kappa_c > 1$.

In Figure 7, we plot the separation between the two outer images as a function of the source location, for various values of κ_c. The plot only extends to $y/y_r = 1$, since larger values of y only produce one image. The separation is fairly insensitive to the source location, and stays within $\sim 15\%$ of the Einstein ring diameter $\Delta x = 2x_t$ for all values of κ_c considered. This is particularly convenient for theoretical studies, when the actual source location can be ignored.

4.2 Magnification and brightness ratios

The magnification of an image located at position x on the lens plane is given by

$$\mu = \left(1 - \frac{m}{x^2}\right)^{-1} \left[1 - \frac{d}{dx}\left(\frac{m}{x}\right)\right]^{-1} = \left(1 - \frac{\alpha}{x}\right)^{-1} \left(1 - \frac{d\alpha}{dx}\right)^{-1} \quad (24)$$

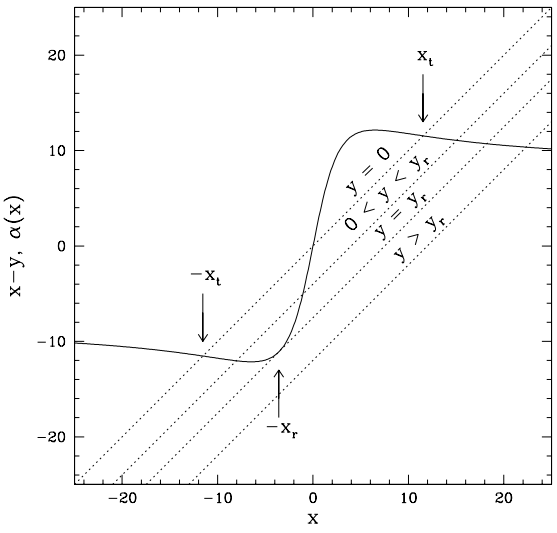

Figure 5. Plot of $\alpha(x)$ (solid curve) and $x - y$ (dotted lines) versus x, for a TIS with $\kappa_c = 5.005$ and 4 particular values of y: $y = 0$ (top line), $y = 4$, $y = y_r = 7.515$, and $y = 12$ (bottom line). Images are located at values of x corresponding to intersections between the lines and the curve. Particular solutions, corresponding to images located on critical curves, are indicated by arrows.

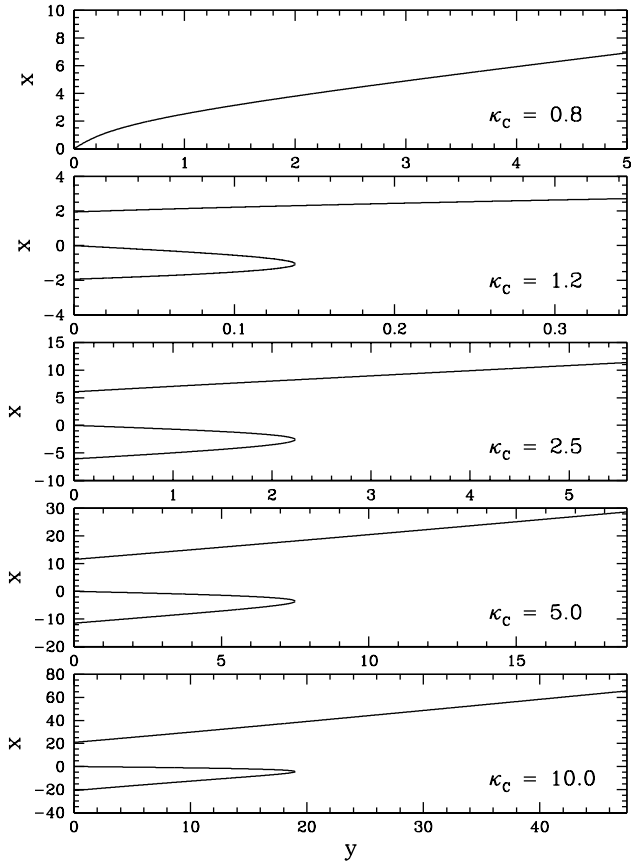

Figure 6. Location x of the image(s) on the image plane versus source location y on the source plane, for various values of κ_c.

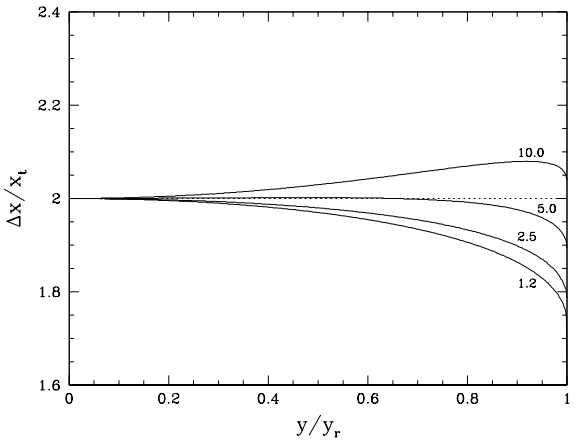

Figure 7. Separation Δx between the two outer images, in units of the tangential critical radius x_t, versus source location y in units of the caustic radius y_r. The solid curves correspond to various values of κ_c, as indicated. The dotted line at $\Delta x = 2x_t$ indicates the diameter of the Einstein ring.

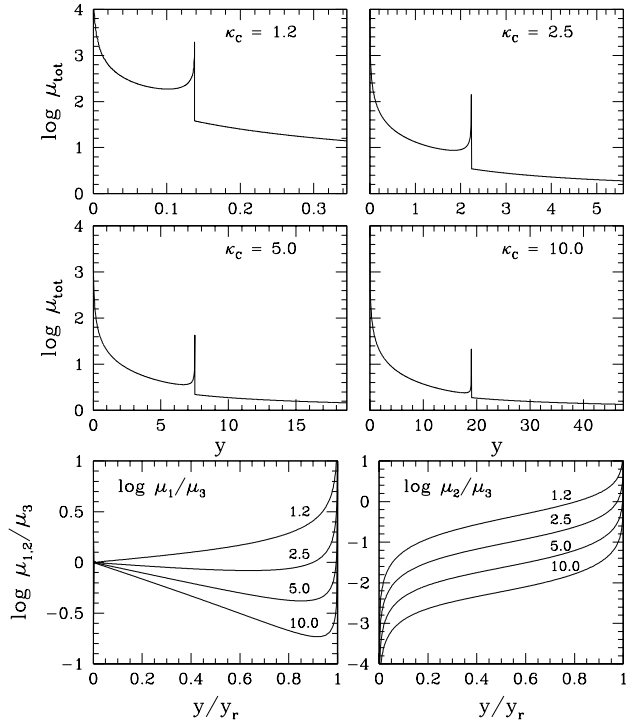

Figure 8. Top four panels: Total magnification $\mu_{\rm tot}$ versus source position y, for four different values of κ_c. Bottom panels: Brightness ratios μ_1/μ_3 and μ_2/μ_3 versus source position in units of caustic radius, y/y_r. The number next to each curve gives the value of κ_c.

(SEF, eq. [8.17]). We computed the total magnification and brightness ratios of images, for the four particular cases $\kappa_c = 1.2$, 2.5, 5.0, and 10.0. The results are shown in Figure 8. The top four panels show the total magnification as a function of the source location y. As y decreases, the magnification slowly increases, until the sources reaches the radial caustic $y = y_r$. At that moment, a second image, with infi-

nite magnification ($1 - d(m/x)/dx = 0$ in eq. [24]) appears on the radial critical curve. As y keeps decreasing, that second image splits into two images, and the total magnification becomes finite again, until the source reaches $y = 0$, and an Einstein ring with infinite magnification ($1 - m/x^2 = 0$ in eq. [24]) appears on the tangential critical curve. Of course, these infinite magnifications are not physical, since they can only occur for point sources.

The total magnification is always larger than unity, and always larger when 3 images are present. Figure 8 shows that the total magnification decreases with increasing κ_c, which seems counter-intuitive. Notice, however, that the top four panels in Figure 8 are plotted for different ranges of y. At a fixed y, the total magnification always increases with κ_c.

The bottom panels of Figure 8 shows the brightness ratios μ_1/μ_3, and μ_2/μ_3, where μ_i is the magnification of image i, as a function of source position. By convention, image 1 is the one between the tangential and radial critical curves, image 2 is the one inside the radial critical curve, and image 3 is the one outside the tangential critical curve (see Fig. 4; from left to right, the three images are image 1, 2, and 3). For most values of κ_c, image 3 is the brightest, image 1 is fainter, but comparable, and image 2 (the central one) is much fainter. This is a generic properties of most axially symmetric lenses with a central core. However, we find a different behavior at small values of κ_c. Not only can image 1 become brighter than image 3, but for a source located at $y \lesssim y_r$, just inside the caustic, even image 2 can become brighter than image 3.

4.3 Shear

The total shear $\gamma(x)$ of an image located at position x is given by

$$\gamma = \left| \frac{m(x)}{x^2} - \kappa(x) \right| , \tag{25}$$

(SEF, eq. [8.15]), where $\kappa(x) \equiv \sigma(x)/\sigma_{\rm crit}$. We substitute equations (9) and (17) into equation (25), and get

$$\gamma = \frac{ab\kappa_c}{Ab - Ba} \left| \frac{2A}{x^2} \left[(a^2 + x^2)^{1/2} - a \right] - \frac{2B}{x^2} \left[(b^2 + x^2)^{1/2} - b \right] - \frac{A}{(a^2 + x^2)^{1/2}} + \frac{B}{(b^2 + x^2)^{1/2}} \right| . \tag{26}$$

[This result was also obtained by Natarajan & Lynden-Bell (1997).] Figure 9 shows γ versus source position y for various values of κ_c. Notice that the indices 1, 2, 3 refer to the individual images, and not the the shear components. The shear increase with κ_c, as expected. At large values of κ_c, γ_1 increase and γ_3 decrease as y increase, while at small κ_c this trend is reversed. γ_2 always increase with y. In the limit $y \to 0$, we get $\gamma_1 = \gamma_3$ and $\gamma_2 = 0$; Images 1 and 3 become identical, while image 2 becomes circular.

4.4 Time delay

For axially symmetric lenses, the deflection potential $\psi(x)$ is defined by $\alpha = d\psi/dx$. From equation (14), we get

$$\psi(x) = \frac{2ab\kappa_c}{Ab - Ba} \left\{ A(a^2 + x^2)^{1/2} - Aa \ln \left[a + (a^2 + x^2)^{1/2} \right] - B(b^2 + x^2)^{1/2} + Bb \ln \left[b + (b^2 + x^2)^{1/2} \right] \right\} . \tag{27}$$

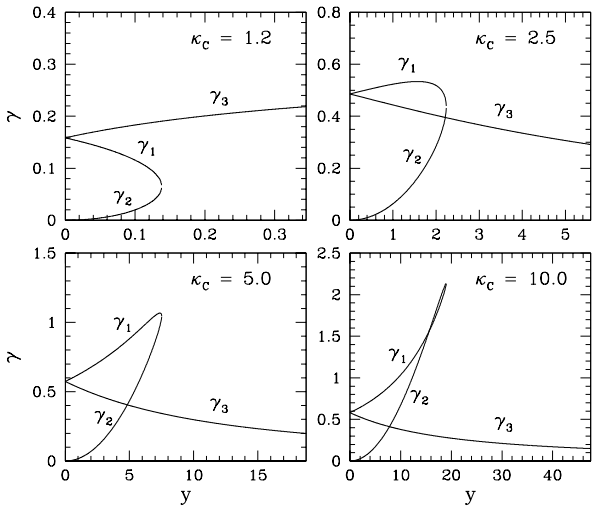

Figure 9. Total shear γ versus source position y, for four different values of κ_c. The indices identify the various images.

The time delay Δt between two images located at x_i and x_j, of a source located at y, is given by

$$\Delta t(y) = \frac{r_0^2 D_S}{c D_L D_{LS}} (1 + z_L) \big[\phi(x_i, y) - \phi(x_j, y) \big] \tag{28}$$

(SEF, eq. [5.44]), where z_L is the redshift of the lens, and $\phi(x, y)$ is the Fermat potential, defined by

$$\phi(x, y) = \frac{1}{2}(x - y)^2 - \psi(x) . \tag{29}$$

In equation (28), the quantities D_S, D_L, D_{LS}, and z_L depend on the redshifts of the source and lens, and the background cosmological model. Only the quantity in square bracket depends on the intrinsic properties of our lens model. We define

$$\tau_{ij} \equiv \phi(x_i, y) - \phi(x_j, y) . \tag{30}$$

Figure 10 shows the time delays as functions of the source location for the cases $\kappa_c = 1.2$, 2.5, 5.0, and 10.0. In all cases, we have $\tau_{23} > \tau_{13} \geqslant 0$. Hence, the light from the three images always reach the observer in the same order, first image 3, then image 1, and finally image 2. As $y \to 0$, $\tau_{13} \to 0$ because images 1 and 3 move toward the tangential critical circle. Both τ_{13} and τ_{23} increase with y, except for small values of κ_c, for which τ_{23} reaches a maximum at some value $y < y_r$, and then decreases slightly. At $y = y_r$, we have $\tau_{13} = \tau_{23}$ because images 1 and 2 merge on the radial critical curve.

An interesting quantity is $\tau_{\rm max}$, the maximum time delay that a lens can produce. For simplicity, we set $\tau_{\rm max} \equiv \tau(y = y_r)$, which, according to Figure 10, is correct for large κ_c, and a fairly good approximation at small κ_c. In Figure 11, we plot $\tau_{\rm max}$ as a function of κ_c. The solution has the following asymptotic behavior,

$$\tau_{\rm max} \approx 8.3(\kappa_c - 1)^2 , \qquad \kappa_c \gg 1 . \tag{31}$$

At small κ_c (but still larger than unity), $\tau_{\rm max}$ exceeds the value given by equation (31).

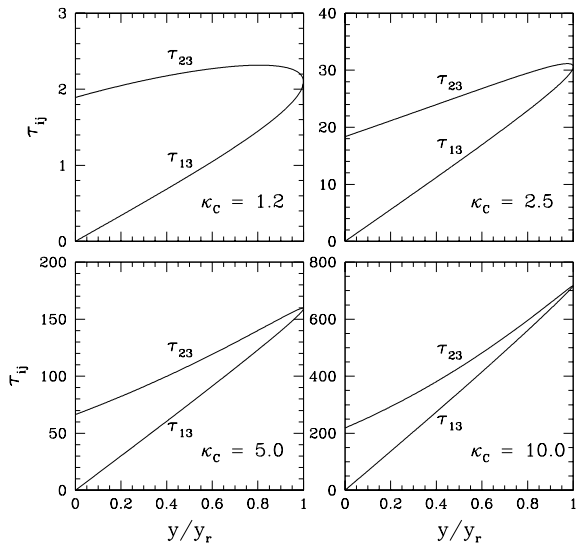

Figure 10. Time delays τ_{12} and τ_{13} versus source position y in units of the caustic radius y_r, for four different values of κ_c.

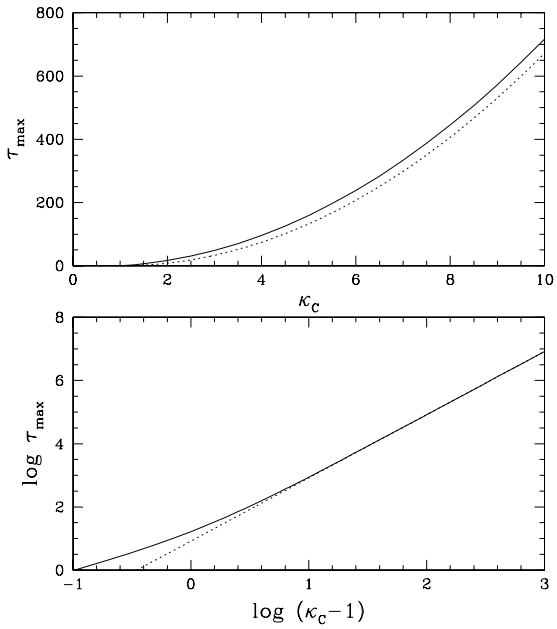

Figure 11. Maximum time delays $\tau_{\rm max}$ versus κ_c, on linear and logarithmic scales (solid curves). The dotted curves show the fitting formula given by equation (31).

5 DISCUSSION

So far, we have focused on the intrinsic, scale-free properties of the lenses, without considering the dependence on the cosmological model. All results have been expressed in terms of two dimensionless parameters, κ_c and y. The cosmological models enter the picture when one tries to determine the typical values and distributions of these parameters. The value of κ_c depends on the critical surface density $\sigma_{\rm crit}$ (eq. [11]), which is a function of the lens redshift, source redshift, and cosmological parameters. In addition, the TIS profile parameters ρ_0 and r_0 are functions of the mass of the object and its epoch of collapse, which also depend upon the cosmological parameters. Finally, the distribution of source locations y will be related to the number densities of sources and lenses, which themselves depend upon the cosmological model.

In this section, we will estimate the typical values of κ_c for TIS halos in a CDM universe. We consider the currently-favored ΛCDM model with density parameter $\Omega_0 = 0.3$, cosmological constant $\lambda_0 = 0.7$, and Hubble constant $H_0 = 70\,{\rm km\,s^{-1}\,Mpc^{-1}}$ (or $h = 0.7$), and we shall assume for illustrative purposes that the source is located at redshift $z_S = 3$. The critical surface density given by equation (11) depends upon the lens redshift z_L, and has a minimum value at $z_L = 0.612$, given by

$$(\sigma_{\rm crit})_{\rm min} = 0.386\,{\rm g\,cm^{-2}}\,. \qquad (32)$$

The surface density of the TIS is computed by plugging the expressions for ρ_0 and r_0 provided in Paper II into equation (9). The central value of the surface density is given by

$$\sigma(\xi = 0) = \pi\rho_0 r_0 \left(\frac{A}{a} - \frac{B}{b}\right)$$
$$= 0.0400[F(z_{\rm coll})]^2 h^{4/3} \left(\frac{M}{10^{12}{\rm M}_\odot}\right)^{1/3} {\rm g\,cm^{-2}}\,. \qquad (33)$$

In equation (33), the function $F(z_{\rm coll})$ is a scaling factor that is used to express the TIS solution for arbitrary cosmological models in terms of the solution for an Einstein-de Sitter model. We will further assume that the lens located at redshift z_L collapsed at redshift $z_{\rm coll} = z_L$.

Let us consider the illustrative case of a lens at $z_L = 0.612$. Using the expressions from Paper II, we get $F(z_{\rm coll}) = 1.1644$. Equation (33), with $h = 0.7$, reduces to

$$\sigma(\xi = 0) = 0.0337 \left(\frac{M_0}{10^{12}{\rm M}_\odot}\right)^{1/3} {\rm g\,cm^{-2}}\,. \qquad (34)$$

Taking the ratio of equations (34) and (32), we get

$$\kappa_c = 0.0874 \left(\frac{M}{10^{12}{\rm M}_\odot}\right)^{1/3}\,. \qquad (35)$$

Since the phenomena of strong lensing (e.g. multiple images, arcs, ...) requires $\kappa_c > 1$, equation (35) indicates that, for our illustrative choice of $(z_L, z_S) = (0.612, 3)$ in a ΛCDM universe, strong lensing requires lensing halos as massive as $M \gtrsim 1.5 \times 10^{15}{\rm M}_\odot$. We can express this more generally by evaluating equations (11) and (33) at different values of $z_L = z_{\rm coll}$ for a given source redshift z_S, as shown in Figure 12. The quantity $\kappa_c(M/10^{15}{\rm M}_\odot)^{-1/3}$ has a maximum value given by

$$\left[\kappa_c M_{15}^{-1/3}\right]_{\rm max} (z_S = 3) = 1.1686\,, \qquad (36)$$

for the ΛCDM universe (which occurs at $z_L = 1.320$), where $M_{15} \equiv M/10^{15}{\rm M}_\odot$. The condition $\kappa_c > 1$, therefore, requires

$$M_{15} \geqslant 0.6266\,. \qquad (37)$$

To see how likely this is, let us focus on our illustrative example of $(z_L, z_S) = (0.612, 3)$. For the cosmological model we consider, a 1-σ density fluctuation collapsing at redshift

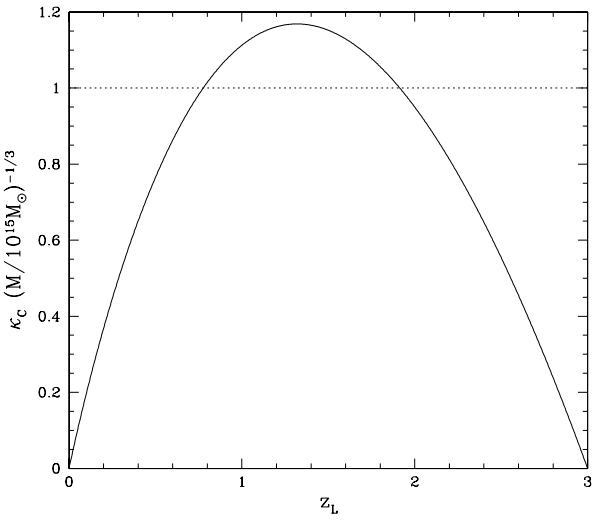

Figure 12. The central convergence κ_c [divided by the factor $(M/10^{15}\mathrm{M}_\odot)^{1/3}$ which contains the dependence on halo mass M] of TIS halos in the ΛCDM universe versus lens redshift z_L, for the illustrative case in which source is located at redshift $z_S = 3$. The horizontal dotted line indicates the minimum value ($\kappa_c = 1$) required for strong lensing by cluster-mass halos of $10^{15}\mathrm{M}_\odot$. (Such halos can only produce strong lensing for $\kappa_c > 1$, i.e. $0.777 < z_L < 1.914$.)

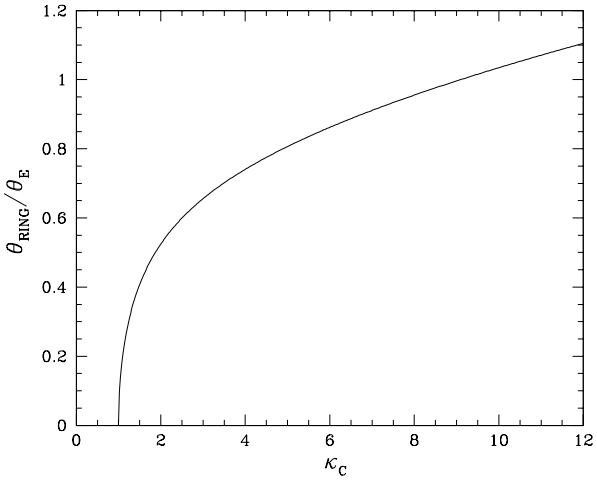

Figure 13. Ratio of the radius $\theta_{\rm ring}$ of an Einstein ring produced by a TIS halo to the radius $\theta_{\rm E}$ of an Einstein ring produced by a Schwarzschild lens of the same mass (the Einstein radius), versus κ_c.

$z_{\rm coll} = 0.612$ has a mass of about $1.5 \times 10^{12}\mathrm{M}_\odot$ (the precise value depends on the details of the power spectrum and its normalization). Such "typical" objects will not be capable of producing multiple images of a source at redshift $z_S = 3$, since the resulting value $\kappa_c = 0.100$ is smaller than unity. This simply indicates that multiple images are not produced by typical objects, which is certainly consistent with the fact that fewer than 100 multiple-image systems have been observed. Increasing κ_c above unity would require an object of mass $M \approx 1.5 \times 10^{15}\mathrm{M}_\odot$, a thousand times the mass of a typical object at that redshift. Clusters of this mass are rare but do exist. We can make a simple estimate of how atypical such a massive object is. Over most of the mass range of cosmological interest (from small galaxies to clusters of galaxies) the CDM power spectrum can be roughly approximated by a power law $P(k) \propto k^n$, where k is the wavenumber and $n \approx -2$. The rms density fluctuation $\delta_{\rm rms}$ is then given by $\delta_{\rm rms} \approx k^{3/2}P^{1/2}(k) \propto k^{1/2}$. At a given redshift, different values of the wavenumber k correspond to different mass scales M according to $M \propto k^{-3}$. The relation between rms density fluctuation and mass scale at fixed epoch is therefore approximated by

$$\delta_{\rm rms} \propto M^{-1/6}\,. \tag{38}$$

Increasing the mass by a factor of 1000 therefore reduces $\delta_{\rm rms}$ by a factor of $1000^{1/6} \approx 3$. Because of the reduction in $\delta_{\rm rms}$, a 1-σ fluctuation ($\delta = \delta_{\rm rms}$) at this higher mass will no longer collapse by this redshift $z_L = 0.612$, but a 3-σ fluctuation ($\delta = 3\delta_{\rm rms}$) will. Such fluctuations are rare, but not vanishingly rare. In Gaussian statistics, the probability that a randomly located point in space is inside a 3-σ density fluctuation (i.e. $\delta \geqslant 3\delta_{\rm rms}$) is 1/384. Of course, whether any halo produced by such a fluctuation will actually produce multiple images will depend on the location of the sources. We carried this simple calculation for illustration purpose only. In a future paper, we will present a detailed calculation of the expected frequency of multiple image systems for comparison with the statistics of observed lensing.

In the TIS model, there is a relationship between the parameters ρ_0 and r_0, and the total mass M of the halo, given by

$$M = 4\pi\rho_0 r_0^3 \tilde{M}_t\,, \tag{39}$$

where $\tilde{M}_t = 61.485$ (Paper I). Using this relation, we can directly estimate the separations between multiple images. The Einstein radius of a lens of mass M is defined as the angular radius θ_E of an Einstein ring produced by a Schwarzschild lens[1] of the same mass,

$$\theta_E = \left(\frac{4GM}{c^2}\frac{D_{LS}}{D_L D_S}\right)^{1/2} \tag{40}$$

(SEF, eq. [2.6a]). This Einstein radius is often used to estimate the characteristic scale of image features caused by strong lensing (e.g. ring radius, radial location of arcs, image separations) and to estimate the size of the region within which the mass which is responsible for that strong lensing must be concentrated. Since lensing halos are not actually point masses, however, the angular radius $\theta_{\rm ring}$ of the actual Einstein ring which results if the source is located along the line of sight through the lens center will usually differ from the Einstein radius θ_E, assuming that the lens mass distribution is actually capable of producing a ring. The angular radius $\theta_{\rm ring}$ of the actual Einstein ring produced by a TIS is given by

$$\theta_{\rm ring} = \frac{r_0 x_t}{D_L}\,, \tag{41}$$

where x_t is the solution of equation (18). We take the ratio of

[1] A point mass.

equations (40) and (41), and use equation (11) to eliminate the angular diameter distances. We get, after some algebra,

$$\frac{\theta_{\rm ring}}{\theta_E} = \left(\frac{\pi}{4}\right)^{1/2} \left(\frac{A}{a} - \frac{B}{b}\right)^{1/2} \tilde{M}_t^{-1/2} \kappa_c^{-1/2} x_t = 0.1565 \kappa_c^{-1/2} x_t \,. \quad (42)$$

In Figure 13, we plot $\theta_{\rm ring}/\theta_E$ as a function of κ_c. A ring can be produced only if $\kappa_c > 1$. The ratio of the actual ring radius to the Einstein radius monotonically increases with κ_c, and exceeds unity for $\kappa_c > 9.096$. Hence, the ring produced by a TIS can be either larger or smaller than the ring produced by a Schwarzschild lens of the same mass, depending on the value of κ_c. In the limit of large κ_c, we have $\theta_{\rm ring}/\theta_E \approx 0.2563 \kappa_c^{1/2}$ according to equations (21) and (42). We saw in §4.1 that in cases of multiple images, the separation Δx between the outermost images is always of order $2x_t$. Hence, $\theta_{\rm ring}$ can be reinterpreted as being one half the separation between images.

6 SUMMARY AND CONCLUSION

We have derived the lensing properties of cosmological halos described by the Truncated Isothermal Sphere model. The solutions depend on the background cosmological model through the critical surface density $\sigma_{\rm crit}$, which is a function of the cosmological parameters and the source and lens redshifts, and the TIS parameters ρ_0 and r_0, which are functions of the mass and collapse redshift of the halo, and the cosmological parameters. By expressing the surface density of the halo in units of $\sigma_{\rm crit}$ and the distances in units of r_0, all explicit dependences on the cosmological model disappear, and the solutions are entirely expressible in terms of two dimensionless parameters, the central convergence κ_c and the scaled position y of the source. We have computed solutions, and we provide either analytical expressions or numerical fits, for the critical curves and caustics, the image separations, the magnification and brightness ratios, the shear, and the time delay. Lensing of a point source by a TIS produces either one or three images, depending on whether the source is located outside or inside the radial caustic. When three images are produced, the central one is usually very faint, being highly demagnified. Degenerate image configurations occur when an extended source overlaps a caustic. Two images are produced when the source overlaps the radial caustic, while an Einstein ring with a central spot is produced when the source overlaps the tangential caustic, which is a single point located at $y_t = 0$. These degenerate cases correspond to maxima of the total magnification, which diverges as the source size goes to zero. When three images are produced, the angular separation between the two outermost images depends strongly on κ_c, but only weakly on the source location.

The lens properties are often qualitatively different at small and large κ_c. For instance, at small κ_c, $\kappa_c \gtrsim 1$, the image separation Δx decreases as source position y increases (i.e. as the projected separation between the source position and the lens center increases) (Fig. 7), the brightness ratio μ_1/μ_3 increases with y (Fig. 8), the shear γ_3 of the outermost image decreases with y, and the time delay τ_{23} decreases with y for $y \lesssim y_r$ (Fig. 10), while these quantities behave differently for large κ_c. This is easily understood. Multiple imaging can only occur when the central surface density $\sigma(0)$ exceeds the critical density $\sigma_{\rm crit}$ (or equivalently $\kappa_c > 1$). Since $\sigma(x)$ is a decreasing function of x, there is a natural scale in the system: the position $x_{\rm crit}$ on the lens plane where $\sigma(x_{\rm crit}) = \sigma_{\rm crit}$. If the lens profile was scale-free, as in the cases of a Schwarzschild lens or a singular isothermal sphere, $x_{\rm crit}$ would be the only length scale in the problem, and the properties of the lens would be self-similar. But the TIS has a characteristic length scale, the core radius r_0, and the existence of this second length scale prevents the solutions from being self-similar.

This paper focused on the intrinsic properties of individual lenses described by the TIS model. It provides all the necessary formula one needs to study gravitational lensing by TIS halos in specific cosmological models. We will present such studies in forthcoming papers. As an illustration here, we applied the TIS model to the currently-favored ΛCDM universe, to calculate the central convergence κ_c expected for TIS halos of different masses and collapse epochs. We found that high-redshift sources (e.g. $z_S \approx 3$) will be strongly lensed by TIS halos (i.e. $\kappa_c > 1$) only for cluster-mass halos. We also calculated the characteristic angular scale of image features produced by strong lensing by TIS halos relative to the Einstein radius θ_E of a lens with the same total mass, for comparison with the results for other lensing halo mass profiles and with observed lensing systems.

ACKNOWLEDGMENTS

This work was supported by NASA ATP Grants NAG5-10825 and NAG5-10826, and Texas Advanced Research Program Grant 3658-0624-1999.

REFERENCES

Binney, J., Tremaine, S., 1987, Galactic Dynamics. Princeton University Press, Princeton
Blandford, R. D., Saust, A. B., Brainerd, T. G., Villumsen, J. V., 1991, MNRAS, 251, 600
Burkert, A., 1995, ApJ, 447, L25
Burkert, A., Silk, J., 1999, in Dark Matter in Astrophysics and Particle Physics, Proceedings of the second International Conference on Dark Matter in Astrophysics and Particle Physics, eds. H. V. Klapdor-Kleingrothaus and L. Baudis, Institute of Physics Publishers, Philadelphia, p. 375
Cole, S., Lacey, C., 1996, MNRAS, 281, 716
Chiba, T., Takahashi, R., 2001, preprint (astro-ph/0106273)
Dresler, A., Smail, I., Poggianti, B. M., Butcher, H., Couch, E. J., Ellis, R. S., Oemler, A., 1999, ApJS, 122, 51
El-Zant, A., Shlosman, I., Hoffman, Y., 2001, ApJ, 560, 636
Evrard, A. E., et al., 2002, ApJ, 573, 7
Evrard, A. E., Metzler, C. A., Navarro, J. F., 1996, ApJ, 469, 494
Fukushige, T., Makino, J., 1997, ApJ, 477, L9
Fukushige, T., Makino, J., 2001a, ApJ, 557, 533
Fukushige, T., Makino, J., 2001b, preprint (astro-ph/0108014)

Ghigna, S., Moore, B., Governato, F., Lake, G., Quinn, T., Stadel, J., 2000, ApJ, 544, 616
Hinshaw, G., Krauss, L. M., 1987, ApJ, 320, 468
Huss, A., Jain, B., Steinmetz, M., 1999, MNRAS, 308, 1011
Iliev, I. T., 2000, PhD Thesis (University of Texas at Austin)
Iliev, I. T., Shapiro, P. R., 2001a, MNRAS, 325, 468 (Paper II)
Iliev, I. T., Shapiro, P. R., 2001b, preprint (astro-ph/0112427)
Jaroszyński, M., 1991, MNRAS, 249, 430
Jaroszyński, M., 1992, MNRAS, 255, 655
Jing, Y., & Suto, Y., 2000, ApJ, 526, L69
Keeton, C. R., & Madau, P., 2001, ApJ, 549, L29
Klypin, A., Kravtsov, A. V., Bullock, J. S., Primack, J. R., 2000, preprint (astro-ph/0006343)
Kochanek, C. S., 1995, ApJ, 453, 545
Li, L.-X., Ostriker, J. P., 2002, ApJ, 566, 652
Moore, B., 2001, in AIP Conf. Series 586, Relativistic Astrophysics, Proceedings of the 20th Texas Symposium, eds. J. C. Wheeler & H. Martel, p. 73
Moore, B., Governato, F., Quinn, T., Stadel, J., Lake, G., 1998, ApJ, 499, L5
Moore, B., Quinn, T., Governato, F., Stadel, J., Lake, G., 1999, MNRAS, 310, 1147
Narayan, R., White, S. D. M., 1988, MNRAS, 231, 97p
Natarajan, P., Lynden-Bell, D., 1997, MNRAS, 286, 268
Navarro, J. F., Frenk, C. S., White, S. D. M., 1996, ApJ, 462, 563
Navarro, J. F., Frenk, C. S., White, S. D. M., 1997, ApJ, 490, 493
Power, C., Navarro, J. F., Jenkins, A., Frenk, C. S., White, S. D. M., Springel, V., Stadel, J., Quinn, T., 2002, submitted to MNRAS (astro-ph/0201544)
Premadi, P., Martel, H., Matzner, R., 1998, ApJ, 493, 10
Premadi, P., Martel, H., Matzner, R., Futamase, T., 2001, ApJ Suppl., 135, 7
Primack, J. R., Bullock, J. S., Klypin, A. A., Kravtsov, A. V., 1999, in ASP Conf. Ser. 182, Galaxy Dynamics, ed. D. R. Merritt, M. Valluri, and J. A. Sellwood (San Francisco: ASP)
Rusin, D., Ma, C.-P., 2001, ApJ, 549, L33
Schneider, P., Ehlers, J., Falco, E. E., 1992, Gravitational Lenses (New York: Springer) (SEF)
Shapiro, P. R., Iliev, I. T., 2001, ApJ, 542, L1
Shapiro, P. R., Iliev, I. T., Raga, A. C., 1999, MNRAS, 307, 203 (Paper I)
Soucail, G., 2001, in AIP Conf. Series 586, Relativistic Astrophysics, Proceedings of the 20th Texas Symposium, eds. J. C. Wheeler & H. Martel, p. 233
Spergel, D. N., Steinhardt, P. J., 2000, Phys.Rev.Lett., 84, 3760
Tormen, G. , Bouchet, F. R., White, S. D. M., 1997, MNRAS, 286, 865
Takahashi, R., Chiba, T., 2001, ApJ, 563, 489
Turner, E. L., Ostriker, J. P., Gott, J. R., 1984, ApJ, 284, 1
Tyson, J. A., Kochanski, G. P., Dell'Antonio, I. P., 1998, ApJ, 498, L107
van den Bosch, F. C., Swaters, R. A., 2001, MNRAS, 325, 1017
Wyithe, J. S. B., Turner, E. L., Spergel, D. N., 2001, ApJ, 555, 504
Young, P., Gunn, J. E., Kristian, J., Oke, J. B., Westphal, J. A., 1980, ApJ, 241, 507

This paper has been typeset from a TEX/ LATEX file prepared by the author.